JAAS

Accepted Manuscript

This is an *Accepted Manuscript*, which has been through the Royal Society of Chemistry peer review process and has been accepted for publication.

Accepted Manuscripts are published online shortly after acceptance, before technical editing, formatting and proof reading. Using this free service, authors can make their results available to the community, in citable form, before we publish the edited article. We will replace this *Accepted Manuscript* with the edited and formatted *Advance Article* as soon as it is available.

You can find more information about *Accepted Manuscripts* in the Information for Authors.

Please note that technical editing may introduce minor changes to the text and/or graphics, which may alter content. The journal's standard Terms & Conditions and the Ethical guidelines still apply. In no event shall the Royal Society of Chemistry be held responsible for any errors or omissions in this *Accepted Manuscript* or any consequences arising from the use of any information it contains.

ROYAL SOCIETY OF CHEMISTRY

www.rsc.org/jaas

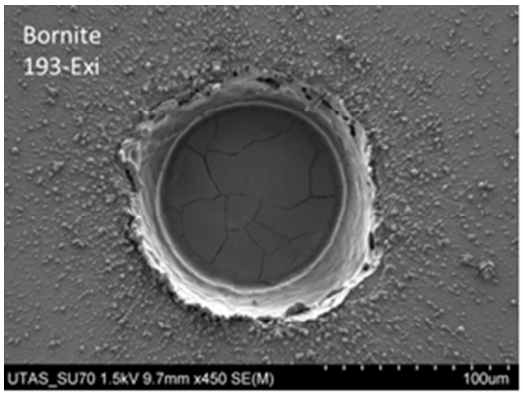

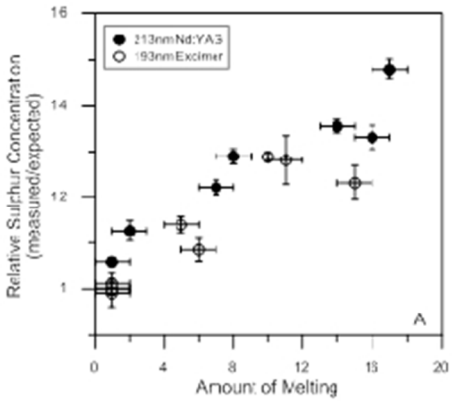

JAAS

RSCPublishing

PAPER

Fractionation of sulphur relative to iron during Laser Ablation-ICP-MS analyses of sulphide minerals: implications for quantification

Cite this: DOI: 10.1039/x0xx00000x

S.E. Gilbert*[a], L.V. Danyushevsky[a], K. Goemann[b], D. Death[c]

Received 00th January 2012,
Accepted 00th January 2012

DOI: 10.1039/x0xx00000x

www.rsc.org/

In this study we investigate the effect that the mineral composition has on the quantification of sulphur by Laser Ablation ICP-MS (LA-ICP-MS) between a range of sulphide minerals: pyrite, pyrrhotite, bornite, chalcopyrite, sphalerite, pentlandite and tetrahedrite. The amount of S fractionation, relative to Fe, was compared between three different nano-second pulse width laser ablation systems: a 213 nm Nd:YAG, a 193 nm Nd:YAG and a 193 nm excimer. Significant matrix effects were seen for some minerals. With the 213nm Nd:YAG laser, the yield (sensitivity per $\mu g.g^{-1}$) of S relative to Fe is up to 50% higher for tetrahedrite and approximately 30% higher for bornite and chalcopyrite when compared to the yields of pyrite, whereas no fractionation was seen between Cu and Fe. For analyses on a fixed position on the sample, significant down-hole fractionation (DHF) occurred where S/Fe ratios increased during an analysis. The rate of DHF is also mineral specific, emphasising the need for matrix matched standards for accurate S analysis. The ablation properties of the minerals were also investigated by characterising the shape of the ablation craters and the composition and morphology of the deposited aerosol material around the ablation site using a field emission scanning electron microscope (FE-SEM). At fluences below 3.5 J/cm^2, pyrite is ablated efficiently by all laser systems with minimal melting around the ablation site, producing steep sided ablation craters. However, some melting occurs in and around the craters for most other sulphide minerals. The amount of melting is mineral specific and primarily dependent on its physical properties (e.g., bond strength and melting point). The greater the extent of melting, the more S fractionation occurs, consistent with the higher volatility of S relative to Fe.

Introduction

LA-ICP-MS has become a widely used analytical technique for trace element and isotopic analysis for a wide range of geological applications.[1-7] It is important to characterise the physical and chemical processes occurring during ablation for accurate analyses and to better understand the limitations of the technique. For geological applications, the ablation mechanics and particle formation processes for zircons and other silicate minerals, glasses and metal alloys have been studied extensively with a range of *ns* and *fs* pulse width lasers.[8-17] However, the ablation mechanisms for pyrite[18] and other sulphide minerals have not been fully characterised to date.

The physical mechanisms for ionisation, atomisation and aerosol formation due to the sample-laser interaction are complex.[10, 11, 19] In some materials the energy from the laser pulse can be dissipated into the sample causing localised heating and melting in and around the laser crater. Following the ablation process, particles can be formed by several mechanisms: [9-12, 15, 20] 1) removal of melt within the ablation crater by the shock wave caused by the expanding laser induced plasma (hydrodynamic sputtering); 2) fracturing and fragmentation of the solid mineral; 3) condensation from the cooling plume of vaporised material; and 4) coalescence of small condensed particles via collision. Elements can be partitioned into different particles dependent on the element volatility, where particles formed later in the ablation process (via late condensation and coalescence) tend to be smaller and enriched in the more volatile elements.[8, 10, 13, 15-17, 19, 21-23] The differences in transport efficiencies of these particles, from the laser sample chamber through the interface tubing to the ICP-MS, and their size-dependent ionisation efficiency in the plasma, can produce element fractionation if the composition of all or some particles are not representative of the sample.[13, 15, 22, 24] For *ns* pulse width lasers, additional fractionation can occur during melting of the material around the ablation crater, via preferential evaporation of volatile elements,[8, 13, 14, 17, 20] whereas for *fs* lasers fragmentation and vaporisation-condensation mechanisms dominate.[10] However, for some materials the fractionation effects between volatile and refractory elements may be reduced by increasing the laser fluence (using a 266nm Nd:YAG laser).[17] Highly volatile elements which may remain in the gaseous state can be fractionated further by condensing on the inner surface of the sample chamber and interface tubing between the laser and ICP-MS.[10, 13, 16, 17, 19, 21-23]

Particle formation processes with all laser types are dominated by the element interactions in the cooling ablation plume, and are common to all wavelengths and pulse widths, including *fs* pulse width lasers, if near complete vaporisation of a sample

occurs.[8, 10, 14, 24] For short pulse width lasers, the ablation plume will be smaller and shorter lived and hence less fractionation would be expected to occur. The laser pulse will interact differently with each material ablated depending on the wavelength and pulse width of the laser and also on the physical properties of the mineral (e.g., bond strength, opacity and heat capacity).[25-27] These differences in the laser-solid interaction, in turn influences the particle forming processes and the amount of element fractionation (matrix effects). With *ns* pulse width lasers, accurate analyses require matrix matching of reference standards and unknowns.[28-31] To date there are few studies[12] of ablation mechanics conducted with shorter wavelength (213 nm & 193 nm) *ns* pulse width lasers, as used here.

Here we present data for the fractionation of S relative to Fe (a volatile versus refractory element) in a range of sulphide minerals: pyrite FeS_2; pyrrhotite $Fe_{1-x}S$; pentlandite $(Fe,Ni)_9S_8$; sphalerite (Zn,Fe)S; chalcopyrite $CuFeS_2$; bornite Cu_5FeS_4; and tetrahedrite $(Cu,Fe,Zn,Ag)_{12}Sb_4S_{13}$. The amount of melting around the craters and the morphology and composition of the particulates surrounding the craters were also investigated. Understanding the fractionation of S and characterising the need for matrix matched standards is essential for accurate S analyses and is of particular importance if S is to be used as an internal standard element[32, 33] or for quantification by summing major elements to 100% totals.[34-36]

Methodology

A range of Fe-bearing sulphide minerals were analysed in this study. Each mineral was set in a 25 mm round epoxy mount, polished and carbon coated. The major element composition and homogeneity were measured with a Cameca SX100 electron microprobe (Central Science Laboratory, University of Tasmania) with a 2 µm beam diameter at 20 kV accelerating voltage and 15 nA beam current (see supplementary material for further details).

Three nano-second pulse width UV lasers were used: a NewWave UP193ss Nd:YAG (UP193), a NewWave UP213 Nd:YAG (UP213) and a Resonetics RESOlution 193nm excimer laser (193-Ex; see Table 1). Each laser system was coupled to an Agilent 7700s ICP-MS. Both Nd:YAG lasers were equipped with in-house constant geometry sample chambers, and the excimer laser with a S-155 large volume constant geometry chamber (Laurin Technic, Australia). Samples were ablated in a He atmosphere and the aerosol mixed with Ar carrier gas before being transported to the ICP-MS. The ICP-MS was tuned for low oxide production (ThO/Th < 0.2 %).

For each mineral, the S concentration was measured by LA-ICP-MS using a pyrite as the reference material and ^{57}Fe as the internal standard element (calculations after Longerich et al, 1996[37]). The analytical conditions used for the reference pyrite for each laser system were kept constant throughout all tests to allow for direct comparison between laser sessions (details are listed in Table 1). The pyrite was measured in triplicate before and after each set of unknowns (up to 18 analyses, ~1 hr) and used to correct for instrument drift. Total acquisition time for each analysis was 90 *s*, consisting of 30 *s* of gas background, acquired with the laser switched off, and 60 *s* of ablation signal. Potential O_2 interferences on ^{32}S and ^{34}S isotopes were minimised by flushing the interface tubing with Ar when the ICP-MS was idle (i.e., overnight) to prevent the ingress of atmospheric O_2 and reduce the instrument stabilisation time after plasma ignition.[38] Both ^{32}S and ^{34}S isotopes were measured and reported concentrations are an average of the two isotopes as they gave consistent concentrations. Other isotopes measured were: ^{57}Fe, ^{59}Co, ^{60}Ni, ^{65}Cu, ^{66}Zn, ^{109}Ag, ^{111}Cd, ^{121}Sb. The dwell times for ^{32}S and ^{34}S were 10 ms, 10-20 ms for other masses, and the total sweep time for all masses was 0.17 sec, giving approx. 350 data sweeps during the 60 *s* analysis.

The depths and cross-section profiles of the ablation craters were measured with a Wyko NT 9100 optical profiler (Veeco, NY, USA). Secondary electron images of the craters and the morphology of the aerosol deposited around each crater were taken with a Hitachi SU-70 field emission SEM (Central Science Laboratory, University of Tasmania) using 1.5 kV accelerating voltage. The elemental composition of the ablated particles was analysed with an Oxford XMax 80 Aztec 2.1 energy dispersive x-ray spectrometer system (EDS). For pyrite and pyrrhotite analyses, pyrite was used as the standard for Fe (Lα) and S (Kα) using 15 kV accelerating voltage. For chalcopyrite analyses, a chalcopyrite was used as the standard for Fe (Kα), Cu (Kα) and S (Kα) at 7 kV accelerating voltage. The analysis totals were generally low due to the surface roughness of the aerosol particles, and only analyses with 90-100% totals were used.

	NewWave UP193ss	NewWave UP213	Resonetics RESOlution
Wave Length	193 nm	213 nm	193 nm
Pulse Width	< 4 ns	< 4 ns	20 ns
Laser Type	Nd:YAG Solid State	Nd:YAG Solid State	ArF excimer
Referred to in text	UP193	UP213	193-Ex
He gas flow rate	0.85 L/min	0.89 L/min	0.35 L/min
Ar gas flow rate	0.91 L/min	0.89 L/min	1.05 L/min
	Analytical conditions for the reference pyrite		
Beam Size	50 µm	47 µm	67 µm
Fluence	2.7 J/cm^2	4.2 J/cm^2	2.7 J/cm^2
Repetition rate	10 Hz	10 Hz	10 Hz

Table 1. Laser Ablation systems used in this study.

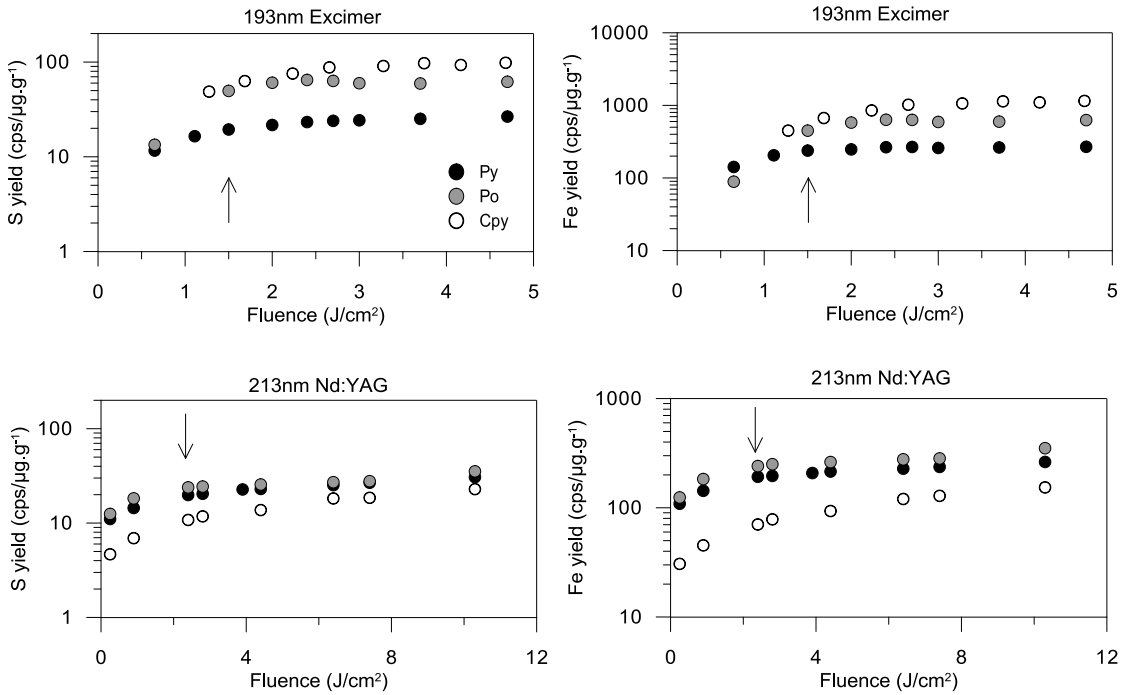

Fig. 1 Fe and S yields (cps/µg.g^{-1}) for pyrite (Py, black), pyrrhotite (Po, grey) and chalcopyrite (Cpy white) with changing laser fluence with the 213nm Nd:YAG and 193nm excimer lasers. The arrow indicates the inflection point for pyrite. Note: for this experiment chalcopyrite was analysed in a different analytical session to the pyrite and pyrrhotite with the excimer laser, and differences in instrument tuning account for the apparent change in relative order of the minerals compared to the 213nm laser.

Results and Discussion

Effects of Laser Energy

The Fe and S yields (cps/µg.g^{-1}) were measured over a range of fluences from 0.2 to 10 J/cm^2 with the UP213 laser and 0.6 to 4.7 J/cm^2 with the 193-Ex laser for pyrite, pyrrhotite and chalcopyrite (Fig. 1). For all minerals there was an increase in the yields with increasing fluence with the most significant rate of change at low fluence. For each mineral there is an inflection point at 2.5-3.0 J/cm^2 with the UP213 laser and at 1.5-2.0 J/cm^2 with the 193-Ex. The ablation conditions for the reference pyrite for each laser were selected at ~1 J/cm^2 above this inflection point where any small fluctuations in fluence during an analysis had little effect on the yields. Higher fluence was not considered ideal for the reference pyrite due to the potential for excessive heating and melting of the mineral around the ablation crater.

Ablation Characteristics of Sulphides

Ablation Crater Morphology: The ablation craters and the morphology of the particulates deposited around these craters were imaged using a FE-SEM. The craters from the UP213 and 193-Ex lasers were ablated with ~100 µm beam size for 300 laser pulses at 4.2 J/cm^2 and 2.7 J/cm^2 respectively. Overall, the 193-Ex laser produces craters with a uniformly flat base, most likely due to homogeneous energy distribution across the laser beam.[39] For most minerals there was enhanced ablation at the edges of the craters with this laser (e.g. Fig. 2A). In contrast the UP213 laser produces a more undulating crater base, most likely caused by irregularities in the laser energy density across the beam where regions of higher fluence would ablate more rapidly (e.g. Fig. 2B; see ESI for additional crater profiles). For both lasers, the pyrite craters were steep sided with minimal melting around the rim of the craters (Fig. 3), similarly for sphalerite with the 193-Ex laser. However, for all other minerals some melting was observed on the base and rim of the craters. The craters in each mineral were ranked based on the amount of melting using the following criteria: roundness of the crater, slope of the walls, evidence of solidified melt on and around the rim and cooling cracks on the base (see ESI for additional information). With both laser systems the relative amount of melting between minerals was consistent: pyrite, sphalerite < pyrrhotite < pentlandite < chalcopyrite < bornite < tetrahedrite.

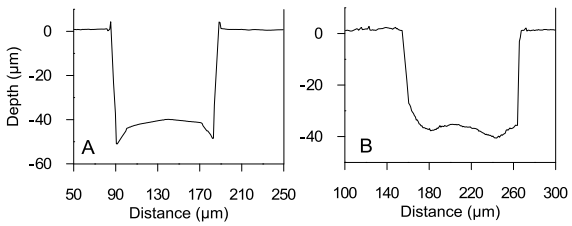

Fig. 2 Examples of representative cross-sectional profiles of the ablation craters: A) in sphalerite with the 193nm excimer laser and B) in pyrite with the 213nm Nd:YAG laser.

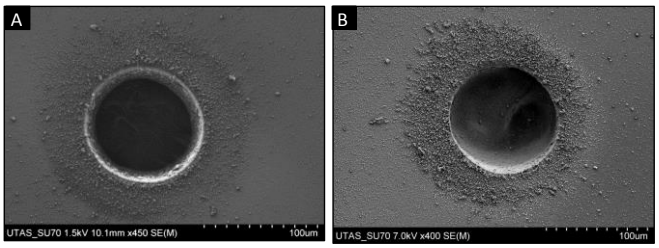

Fig. 3 Secondary electron images of pyrite craters from: A) the 193nm excimer laser and B) the 213nm Nd:YAG laser.

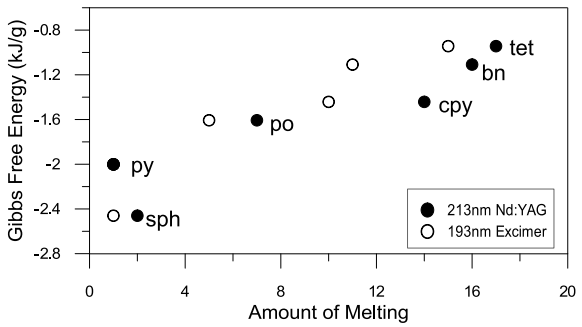

Fig. 4 Relationship of Gibbs Free Energy with the amount of melting in and around the ablation crater. Bornite (bn); chalcopyrite (cpy); pyrite (py); pyrrhotite (po); sphalerite (sph); tetrahedrite (tet). Values for Gibbs Free Energy from Wagner et al (2002)[27] and Kelley & Fallick (1990).[25]

A minerals bond strength can be estimated by the Gibbs Free Energy of formation at standard pressure and temperature, where the higher the Gibbs Free Energy, the weaker the bond strengths.[25, 27] Figure 4 shows that higher amounts of melting occurred for minerals with weaker bond strengths. We propose that the amount of melting is primarily dependent on the physical properties of that mineral (e.g., bond strengths, melting point and thermal conductivity) rather than the wavelength or pulse width of the laser, due to similarities in behaviour of the minerals with both laser systems. Increasing the laser fluence would be expected to create larger amounts of melting overall, however, the relative order of the minerals is likely to remain the same for a given fluence, as the physical properties of the minerals are constant.

Ablated Aerosol Morphology

The morphology of the ablated material surrounding the craters can differ between UP213 (at 4.2 J/cm^2) and the 193-Ex (at 2.7 J/cm^2) despite similar amounts of melting occurring for each mineral. Three main particle morphologies were observed for the sulphide ablations (Fig. 5): Type 1) large (approx. 0.1-1.0 µm) solidified droplets of molten material, either spherical or spattered depending on the distance from the ablation crater and the melting point of the mineral; Type 2) small (approx. 20-100 nm) round particles formed by condensation of the ablation plume; and Type 3) diffuse clusters of very fine condensate. Large particles are most abundant close to the ablation craters, and it is unlikely that they are transported to the ICP-MS due to their size. If the compositions of the smaller particles (Types 2 and 3) vary, with the clusters of finer particles being enriched in volatile elements,[10, 13, 17, 19] this would result in fractionation of S relative to Fe due to the differences in their transport efficiencies through the interface tubing and ionisation in the plasma.[13, 15, 22, 24]

In general the 193-Ex laser produces finer particles than the UP213 laser, due to the shorter wavelength and more efficient ablation.[22] However, the morphology of the ablated material can differ for some minerals between the two laser wavelengths. At the laser fluences tested, pyrite, chalcopyrite and pyrrhotite produce similar particle types with both laser systems (Fig. 5 I-K), whereas bornite, pentlandite, sphalerite and tetrahedrite produce material with differing morphologies (Fig. 5A-H). The particle size and morphologies for pyrite and pyrrhotite were similar for each mineral over a range of fluence with the UP213 laser (0.5-10 J/cm^2), but the lateral extent and thickness of the material around the craters was significantly greater at high fluence. These similarities in morphology, regardless of fluence suggest any differences seen between the laser systems are related to both mineral type and laser wavelength, rather than fluence.

Other less common particulates were also observed, in addition to the predominant particle types mention above. For chalcopyrite, bladed crystals of bornite formed on the base and rim of the crater and occasionally on the tops of large round particles, with both laser systems (Fig. 5J). These crystals always occurred above solidified melt rather than on areas rich in condensate. Therefore, they must form late in the cooling process during solidification. Elongated, rope-like clusters of condensate (up to 1.5 µm in length) occurred around the tetrahedrite craters (Fig. 5D), and ripples occurred in the very fine particulates surrounding the sphalerite craters with the UP213 laser (Fig. 5C). These ripples were uniformly orientated regardless of their relative position to the crater, suggesting that they were likely caused by a preferential flow direction of the He gas at the ablation site, rather than the shockwave associated with the ablation process.

Ablated Aerosol Composition

Pyrite and pyrrhotite were ablated with 100 µm beam size for 300 laser pulses at 4.2 J/cm^2 with the UP213 laser. The Fe and S composition of the melted material on the crater rims and the particles surrounding the craters were measured by EDS. For pyrite (FeS_2), the melt material on the crater rims and the condensate clusters (Type 3 particles) surrounding the crater were depleted in S (Table 2). The melted material surrounding the pyrrhotite (FeS) crater retained the Fe-S ratio of the initial pyrrhotite (i.e., no loss of volatile S) despite significantly more melting during ablation. The upper temperature limit for pyrite stability is 743 ^oC where it decomposes to pyrrhotite (FeS)[18, 40] i.e., $FeS_2 \rightarrow FeS + S_{(g)}$. Thus, during the initial stages of pyrite ablation, rapid heating of the base and walls of the crater may release S in the gaseous state. Conversely as the ablation plume cools, FeS particulates will be formed initially and S will either condense later and be enriched in the finer condensate clusters or may remain in the gaseous state (i.e., as SO_2). [10, 13, 16, 17, 19]

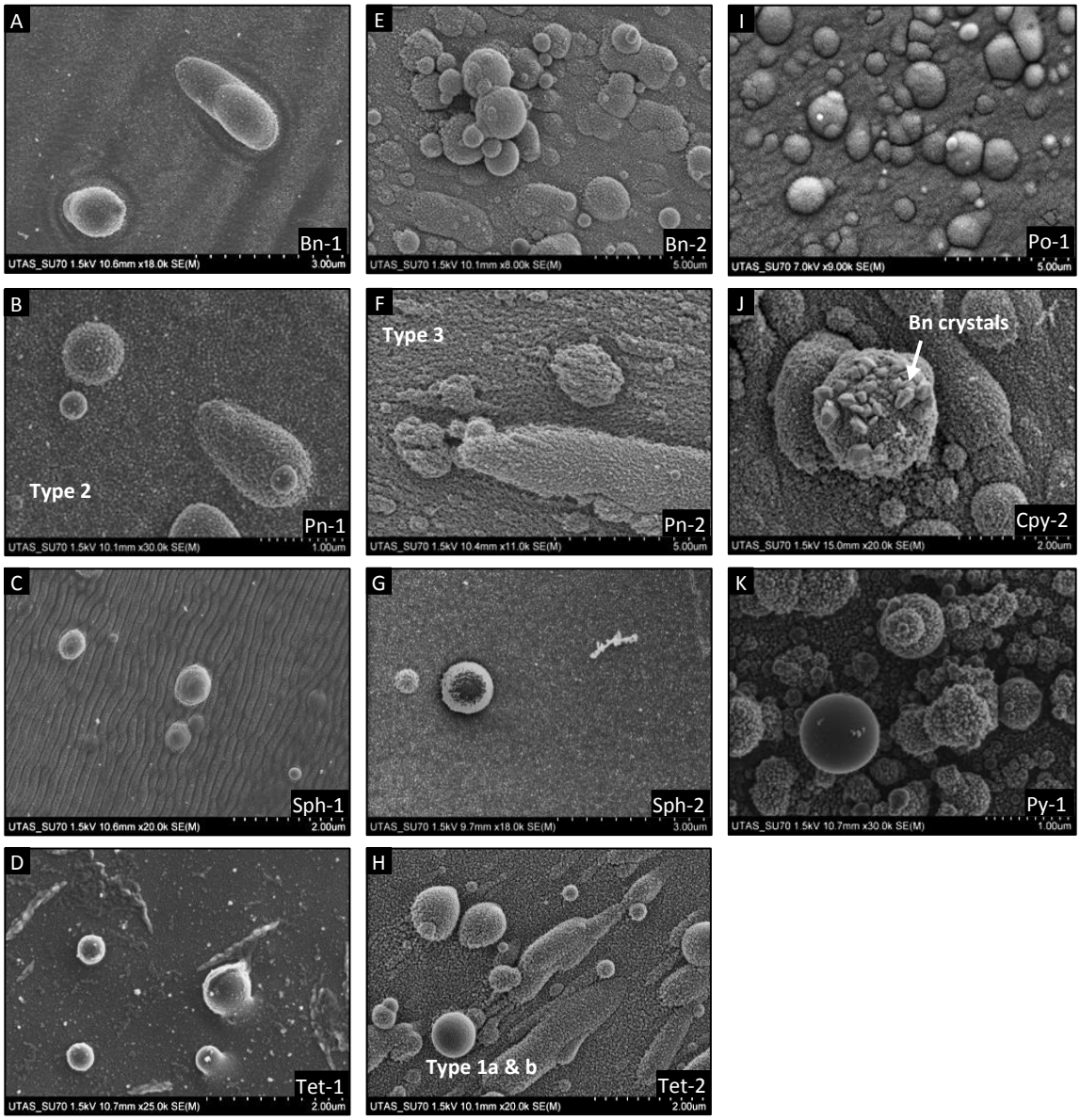

Fig. 5 Secondary electron images of material surrounding the ablation craters. Mineral-1: 213nm Nd:YAG laser at 4.2 J/cm^2 (A-D, I, K); Mineral-2: 193nm excimer laser at 2.7 J/cm^2 (E-H, J). Particle Type 1a & 1b: rounded and spattered droplets; Type 2: small spherical condensate particles coating larger droplets; Type 3: coating of diffuse condensate clusters. Bornite (Bn); chalcopyrite (Cpy); pentlandite (Pn); pyrite (Py); pyrrhotite (Po); sphalerite (Sph); tetrahedrite (Tet).

	av S wt%	av Fe wt%	S/Fe	%RSD	n
Pyrite	53.5	46.5	1.15	1.1	6
Fine condensate	51.8	48.2	1.07	1.8	20
Melted ejecta	41.0	59.0	0.70	8.7	19
Melt on crater rim	44.6	55.4	0.80	8.8	10
Pyrrhotite	39.1	60.9	0.64	0.2	3
Fine condensate	38.0	62.0	0.61	1.4	20
Melted ejecta	38.4	61.6	0.62	3.0	19
Melt on crater rim	39.3	60.7	0.65	2.5	10

Table 2. Concentrations of S and Fe in solidified melt and ablated particulates surrounding the ablation craters in pyrite and pyrrhotite.

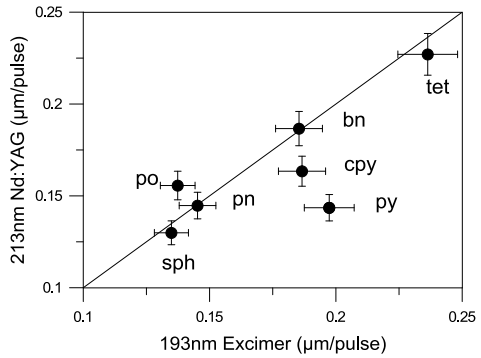

Fig. 6 Ablation rate (µm/pulse) for the 213nm Nd:YAG and 193nm excimer lasers at 4.2 and 2.7 J/cm^2, respectively. Error bars are ±5%, line is 1:1 relationship. Bornite (bn); chalcopyrite (cpy); pentlandite (pn); pyrite (py); pyrrhotite (po); sphalerite (sph); tetrahedrite (tet).

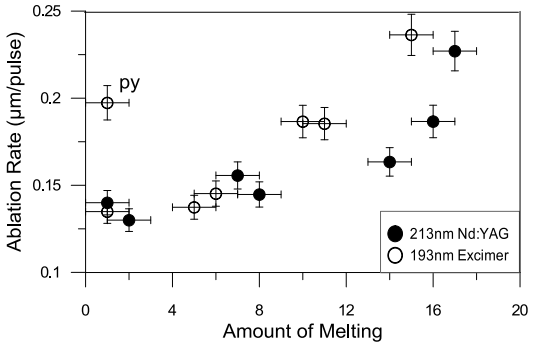

Fig. 7 Relationship between ablation rate (µm/pulse) and amount of melting with the 213nm Nd:YAG and 193nm excimer lasers. Note: anomalously high ablation rate for pyrite (py).

Ablation Rate

The ablation rate for each mineral was calculated by measuring the depth of the crater produced with 300 laser pulses (10 Hz, 30 *s* ablation) at 4.2 and 2.7 J/cm^2 for the UP213 and the 193-Ex lasers, respectively. The ablation rate is similar between the two lasers at these fluences for sphalerite, pentlandite, bornite and tetrahedrite, however, pyrite ablation with the 193-Ex laser produces significantly deeper holes than the UP213 laser (Fig. 6). There is a correlation between the ablation rate and the amount of melting with both lasers for all minerals, with the exception of pyrite with the 193-Ex laser (Fig. 7).

The relatively high ablation rate for pyrite with the 193-Ex laser implies more efficient ablation, where energy loss through melting is minimised. In contrast, for other minerals the ablation rate and hence the depth of the craters, are dependent on the amount of heat transfer and melting in the base of the crater.

Fe and S yields

The LA-ICP-MS yields of Fe and S are dependent on a number of factors including the laser conditions (i.e., beam size, wavelength, pulse frequency and fluence), mineral ablated, interface tubing type and configuration, aerosol transport efficiency and ICP-MS tuning parameters. For all measurements the interface tubing configuration and ICP-MS tuning parameters were the same, hence any differences in yields between minerals for a given laser are due to differences in the ablation characteristics or efficiency of transport. The Fe yields were significantly higher than S both laser systems, due to the differences in ionisation efficiency in the ICP (first ionisation potential 7.9 and 10.4 eV respectively; Table 3). There is a weak correlation between the S/Fe ratios between the two lasers with pyrite, sphalerite < pyrrhotite, pentlandite < bornite, chalcopyrite, tetrahedrite. The 193-Ex laser gave higher yields for both elements, however, the UP213 laser gives higher S/Fe ratios. This implies the S is transported more efficiently relative to Fe with the UP213 laser. The ratios are significantly lower for pyrite with both lasers compared to other minerals, which implies especially low transport efficiency for S from pyrite.

	213 nm Nd:YAG laser			193nm excimer laser		
Mineral	**Fe yield**	**S yield**	**S/Fe *100**	**Fe yield**	**S yield**	**S/Fe *100**
Pyrite	656	64	9.8	3403	167	4.9
Sphalerite	365	41	11.3	3769	189	5.0
Pyrrhotite	394	45	11.5	1618	94	5.8
Pentlandite	273	35	12.9	1862	99	5.3
Bornite	239	31	13.1	2461	159	6.5
Chalcopyrite	299	39	13.2	2159	143	6.6
Tetrahedrite	419	62	14.9	2679	166	6.2

Table 3. Fe and S yields (cps/µg.g^{-1}) for the Nd:YAG 213nm (4.2 J/cm^2) and 193nm excimer (2.7 J/cm^2) lasers. Sensitivity (cps) normalised to 100% isotope abundance. Note, the 213 nm cps measured with a 47 µm beam size and calculated to 67 µm equivalent by area for comparison with the excimer laser.

Sulphur Backgrounds

Sulphur can have a long residence time (washout time) in the laser ablation system creating elevated backgrounds and potential cross contamination between samples.[41, 42] Using a straight piece of nylon tubing (2.6 mm ID, ~3 m length) between the 193nm Nd:YAG (UP193) laser sample chamber and the ICP-MS, the washout time for Fe is ~1 sec. However, the washout time for S when ablating pyrite is >120 *s* compared to ~3 *s* when ablating pyrrhotite (with the same analytical conditions; Fig. 8A). For pyrite, the initial rate of signal drop for S is comparable, but after ~0.5 *s* the rate slows dramatically. This behaviour is not observed with S washout after ablating other minerals. The washout time for S in pyrite was significantly improved (to ~20 sec) by adding: 1) a 'squid' smoothing device (Laurin Technic, Australia) where the sample aerosol is divided between ten tubes of different lengths before being recombined and delivered to the ICP-MS plasma, and 2) a coiled tube[43] (Tygon, 1.5 mm ID, 300 mm length) into the interface tubing between the laser and ICP-MS.

The distinct behaviour of S washout for pyrite implies a different transport mechanisms for S compared to other sulphides. We propose that for pyrite, the observed net S loss from the material surrounding the ablation crater (as measured by EDS; Table 2) is transported to the ICP-MS in the gaseous state or as ultra-fine condensates. Sulphur in these forms could interact and adhere more with the inner surfaces of the interface tubing, compared to the larger FeS particulates,[41] and cause the lower yields for pyrite. This adsorbed S can then be slowly remobilised by the Ar and He carrier gases creating the shoulder and extended washout time for S as seen in Figure 8A.

The squid mixing device reduces the remobilisation of adsorbed S and improves the washout time, via changing flow dynamics as the carrier gas is split from one tube into ten tubes of the same inner diameter. However, the physical mechanisms that control this require further investigation.

The initial rapid drop of S after pyrite ablation is likely to be caused by the washout of larger FeS particulates. The squid mixing device and the coiled tube in the interface smooths the signal and extends the washout time for these particulates (i.e., Fe washout time to ~8 sec, Fig. 8B). However, this was considered insignificant when compared to the overall improvement in S washout.

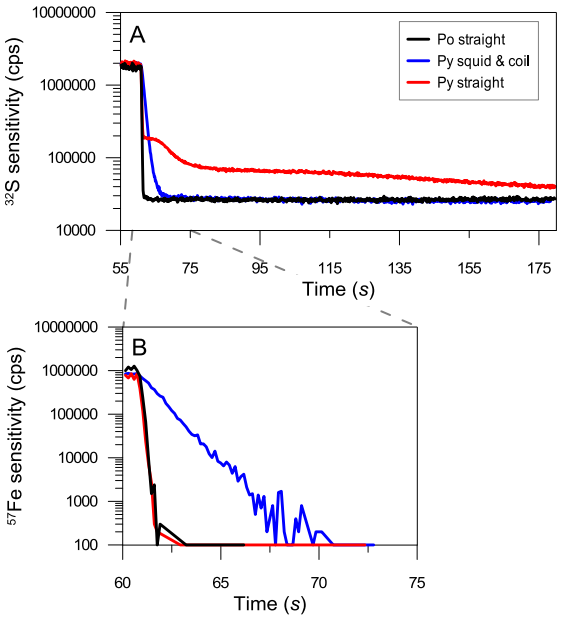

Fig. 8 Signal washout for A) ^{32}S and B) ^{57}Fe, after ablation of pyrite and pyrrhotite with either a straight tube or with the squid and coiled tube mixing devices, between the laser ablation sample cell and the ICP-MS. Laser ablation ended at 61 *s*. Pyrite (Py); pyrrhotite (Po). Notes: three separate ablations have been overlain for comparison in each plot; the first part of the analysis including the background and ablation signal have not been included for clarity; and expanded time scale for Fe washout.

Sulphur Concentration by LA-ICP-MS

The concentration of S was measured by LA-ICP-MS and compared against the electron microprobe results (Table 4). All analyses used the standard conditions listed in Table 1, with line rasters traversing at 3 um/s to negate any down hole fractionation effects common with spot analyses.[39, 44] Using pyrite as the reference material, the results for other minerals are indicative of the amount of S and Fe fractionation relative to their behaviour during the pyrite ablation. With the UP213 laser, the Co-rich pyrite was the only mineral to give consistent results with the reference pyrite (Fig. 9), and with the 193-Ex laser the Co-pyrite, sphalerite and pentlandite were consistent within 10%. For all other analyses significant fractionation was observed (>10 %), especially for chalcopyrite, bornite and tetrahedrite. Overall the UP213 laser has higher fractionation for all minerals, than the 193nm lasers. The shorter pulse width UP193 laser (<4 ns) has less fractionation than the 193-Ex laser (20 ns), for the minerals tested.

Mineral	Fe	S
Pyrite	46.3	53.7
Co-Pyrite	45.1	53.6
Pyrrhotite	61.0	39.0
Sphalerite	6.8	33.3
Pentlandite	29.6	33.4
Chalcopyrite	29.9	35.1
Bornite	11.1	26.2
Tetrahedrite	5.5	25.5

Table 4. Fe and S concentrations (wt%) of sulphide minerals analysed by Electron Microprobe.

The concentrations for Co, Ni and Cu, calibrated against the STDGL2b2 in-house reference material,[30] were within 5% of the expected concentrations for the Co-pyrite (1.5 wt% Co), pentlandite (35.6 wt% Ni), bornite (63.3 wt% Cu), chalcopyrite (34.7 wt% Cu) and tetrahedrite (36.2 wt% Cu). However, significant fractionation of Zn, Ag and Sb occurred in the sphalerite and tetrahedrite with calculated concentrations 1.3-2.0 times higher than expected (see ESI for details). Fractionation of Zn relative to Fe in sphalerite has been previously reported[30] to a similar extent, with measured concentrations 1.3-1.6 times higher than expected, compared to 1.5-1.6 times in this study.

There is a correlation between the amount of melting around the ablation craters and the fractionation of S for both the 193-Ex and UP213 lasers (Fig.10A). A relationship between sulphide bond strength (Gibbs Free Energy) and the degree of S isotopic fractionation (i.e., ^{34}S/^{32}S) during laser combustion isotope analyses has previously been demonstrated.[25, 27] A similar relationship for the fractionation of S and Fe during LA-ICP-MS analyses is shown in Figure 10B. Therefore, the behaviour of S relative to Fe is primarily dependent on the physical properties of the sulphide mineral rather than the type of laser system used.

The concentrations of S in pyrite, pyrrhotite, chalcopyrite and bornite were measured over a range of fluence for the UP213 and 193-Ex lasers (Fig. 11). More fractionation was seen across the range of fluence tested for the 193-Ex laser, especially at low fluence. Each mineral behaves similarly between the two laser systems, where the positive slope for pyrite contrasts to the other minerals. There are two ablation mechanisms for S fractionation relative to Fe, which could account for these differences: a) for minerals where melting occurs around the craters (e.g., pyrrhotite, bornite and chalcopyrite) volatile S can be released by evaporation from molten material. At low fluence, heating and melting rather than ionisation and ablation, becomes the dominant process and hence increases the relative S concentration; and b) for pyrite which has efficient ablation even at low fluence, volatile S can remain in the gaseous state during the condensation process via the cooling reaction $Fe_{(g)} + 2S_{(g)} \rightarrow FeS_{(s)} + S_{(g)}$. The higher the fluence, the higher the temperature and larger the volume of the laser induced plasma following ablation. This would create longer cooling times for the ablation plume, which could increase the likelihood of S partitioning into either the vapour phase or very fine particulates, relative to refractory Fe.

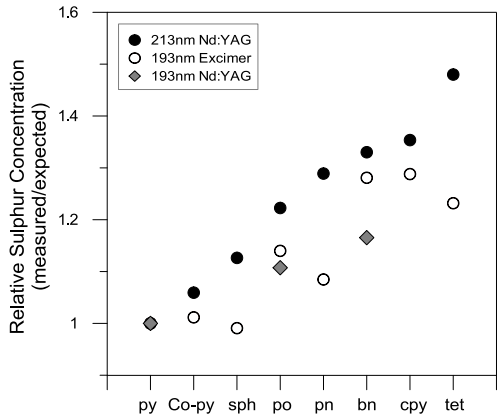

Fig. 9 Concentrations of S measured by LA-ICP-MS relative to the expected concentration (see Table 4). Pyrite was used as the reference material and by definition has a relative S concentration of 1.0 for all laser systems. Note, only pyrite, pyrrhotite and bornite were analysed by the 193nm Nd:YAG laser. Bornite (bn); chalcopyrite (cpy); Co-bearing pyrite (Co-py); pentlandite (pn); pyrite (py); pyrrhotite (po); sphalerite (sph); tetrahedrite (tet).

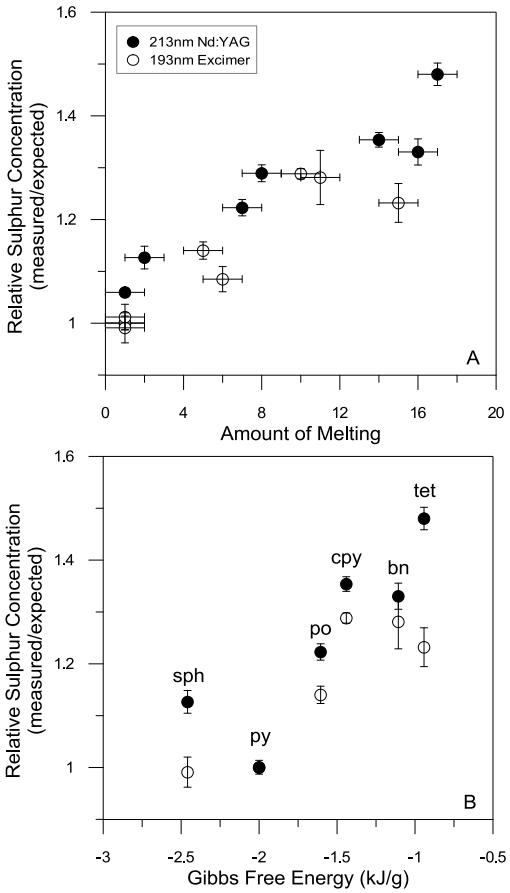

Fig. 10 A) The relationship between the amount of melting on the base and rim of the ablation craters and S fractionation for the 213nm Nd:YAG and 193nm excimer lasers; B) Relationship between Gibbs Free Energy and S fractionation. Bornite (bn); chalcopyrite (cpy); pyrite (py); pyrrhotite (po); sphalerite (sph); tetrahedrite (tet).

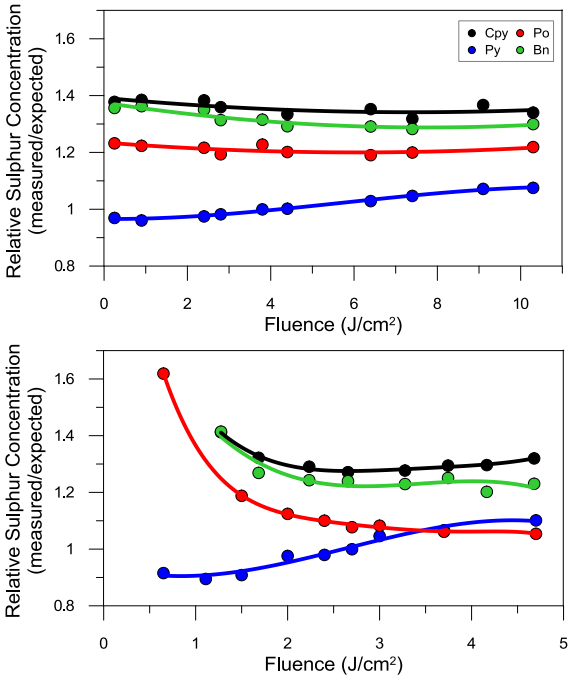

Fig. 11 Influence of laser fluence on S fractionation with the 213nm Nd:YAG and 193nm excimer lasers. Pyrite analysed at 4.2 and 2.7 J/cm^2 respectively, were used as the reference for calibration (relative S concentration = 1.0). Bornite (Bn); chalcopyrite (Cpy); pyrite (Py); pyrrhotite (Po).

The matrix effects between minerals, as defined by the difference between the relative S concentrations (Fig. 11), are greater than the variations with fluence for an individual mineral with the UP213 laser. With the 193-Ex laser the effects of fluence are more significant. The pyrite and pyrrhotite curves overlap at high fluence, meaning that pyrite could be used as an accurate standard for S in pyrrhotite (and vice versa) if they were analysed at higher fluence. The matrix effects of chalcopyrite and bornite cannot be mitigated with changing laser fluence, and matrix matched standard are essential for accurate analyses of these minerals.

Down Hole Fractionation

Down hole fractionation (DHF) is the relative change in yield between elements during a laser ablation spot analysis and is caused by the increasing depth to diameter ratio of the ablation crater with time.[44, 45] DHF was calculated as the average S/Fe cps ratio during the first 5 *s* of the analysis divided by the average ratio during the last 5 sec.[39] When ablating spot analyses, the initial (first 5 sec) S/Fe ratio of the signal is comparable to the ratio of line analyses with the same analytical conditions. For all minerals the Fe sensitivity dropped more rapidly than S, resulting in an increasing S/Fe ratio with time. The amount of DHF is mineral dependent and increases with decreasing spot size (Fig. 12). DHF of S/Fe was most significant for chalcopyrite, but in contrast the Cu/Fe DHF was <4% for all spot sizes measured. The volatility of Fe and Cu are more similar than for Fe and S, therefore they behave more similarly during ablation.

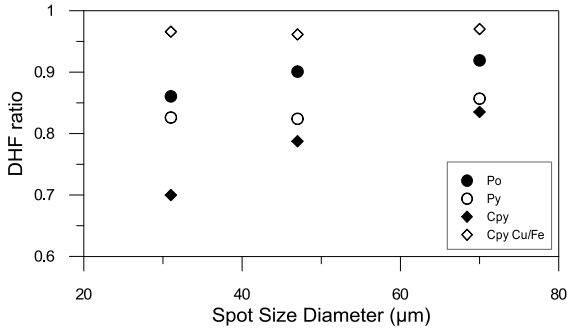

Fig. 12 Dependence of DHF with laser spot size, 213nm Nd:YAG laser. DHF ratio = average S/Fe ratio during the first 5 *s* of the analysis divided by the average ratio during the last 5 sec. All DHF ratios for S/Fe except for Cu/Fe for chalcopyrite (open diamond). Chalcopyrite (Cpy); pyrite (Py); pyrrhotite (Po).

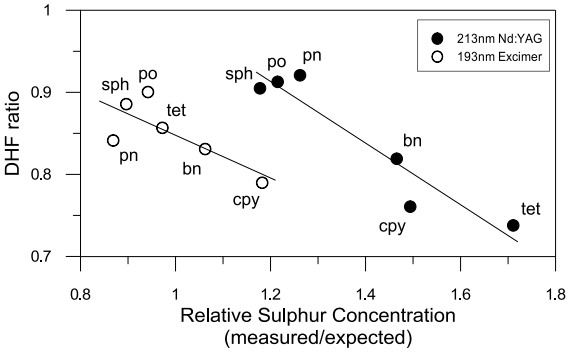

Fig. 13 Relationship of DHF and S fractionation, relative to pyrite reference standard, for spot analyses with the 213nm Nd:YAG (47 μm, 4.2 J/cm^2) and the 193nm excimer (67 μm, 2.7 J/cm^2) lasers. Bornite (bn); chalcopyrite (cpy); pentlandite (pn); pyrrhotite (po); sphalerite (sph); tetrahedrite (tet).

The calculated concentration for a given mineral is dependent on both the mineral-specific matrix effects as seen with line ablations, and the mineral specific DHF. For example, if the increase of S/Fe with time is steeper for a given minerals than for pyrite, the calculated S concentration will be further overestimated for spot analyses. This is the case for chalcopyrite, bornite and tetrahedrite with the UP213 laser (Fig. 13). The DHF ratio for pyrite with the 193-Ex laser was steeper than with the UP213 laser (DHF ratio of 0.79 and 0.84 respectively), and steeper than all other minerals except chalcopyrite, resulting in the relative S concentrations for spot analyses being systematically lower (Fig. 13). This is caused by the relatively fast ablation rate for pyrite with the 193-Ex laser (Fig. 7), creating a deeper hole and increased DHF for the same ablation time.

The fractionation effects between some minerals can be reduced at high fluence (Fig.11), but the ablation rate will also increase as will the degree of DHF. Therefore, using matrix matched standards is particularly important for spot analyses as using high fluence is not recommended. The calculated concentration for S can vary depending on the time interval chosen for integration due to the changing S/Fe ratio with time. For example, for chalcopyrite the calculated concentrations using the first 10 *s* of an analysis can be 10% lower than the concentration calculated over the full 50 *s* analysis. For accurate S analysis it is important to integrate over the same time intervals showing the same amount of DHF in both the standard and sample analyses.

Conclusions

Significant fractionation of S relative to Fe (and Co, Ni, Cu) occurs in all sulphides during LA-ICP-MS analysis, and we propose this is due to the higher volatility of S. The extent of the S fractionation, is dependent on the amount of melting around the ablation crater, which is predominantly mineral specific (e.g., related to bond strengths, melting point and thermal conductivity) rather than dependent on the laser wavelength or pulse width (ns). Although in theory S fractionation could be reduced using a femtosecond laser, due to the potential for reduced melting around the laser craters,[1, 46] this remain untested for sulphide minerals and is the subject of future studies.

Fractionation of volatile S occurs during both the initial stages of ablation with evaporation from heating and melting of the mineral in and adjacent to the crater, and in the condensation stage where volatile elements are partitioned into the smaller particulates or remains in the gaseous state. The latter is particularly evident during pyrite ablation, where the release of gaseous S can account for both the S depletion in the particulate aerosol, and in the long washout time for S after ablation from interaction with the inner surfaces of the interface tubing. Pyrite is also unusual compared to the other minerals tested due to a) more efficient ablation and less melting, b) faster ablation rate with the 193nm excimer laser causing increased down hole fractionation for spot analyses, and c) an increase in S volatility and fractionation relative to Fe at high fluence, rather than at low fluence as for all other mineral tested.

For both 213 nm and 193 nm nanosecond pulse width lasers, using a matrix matched standard is necessary for accurate S analyses in sulphide minerals, especially if S is to be used as the internal standard element or when quantifying by summing major elements to 100% totals. This is particularly important for spot ablations, where there can be significant down hole fractionation of S/Fe, and integrating over the same ablation time for standards and samples is important for accurate quantification.

Acknowledgements

The authors would like to thank Agilent Technologies for their funding support for this project through their University Relations Program. This research was also conducted under the ARC Centre of Excellence funding program to CODES. Thank you to Paul Olin for reading and commenting on early versions of this article and the anonymous reviewers for their valuable comments.

Notes and references

[a] *CODES, University of Tasmania, Australia*
[b] *Central Science Laboratory, University of Tasmania, Australia*
[c] *Agilent Technologies, Melbourne, Australia*
E-mail: sgilbert@utas.edu.au

Electronic Supplementary Information (ESI) available:
Electron microprobe analytical conditions.
Crater cross-sections for all minerals measured by optical profiler.
Major element concentrations measured by Electron Microprobe and LA-ICP-MS.
Criteria for determining the amount of melting around the ablation craters.
See DOI: 10.1039/b000000x/

1. M. Shaheen, J. Gagon and B. J. Fryer, *Chemical Geology*, 2012, **330-331**, 260-273.
2. J. S. Becker, *JAAS*, 2002, **17**, 1172-1185.
3. F. Vanhaecke, L. Balcaen and D. Malinovsky, *JAAS*, 2009, **24**, 863-886.
4. P. J. Sylvester, *Laser ablation ICPMS in the earth sciences: current practices and outstanding issues*, Mineralogical Association of Canada, Vancouver. 2008.
5. R. Large, L. Danyushevsky, C. Hollit, V. Maslennekov, S. Meffre, S. Gilbert, S. Bull, R. Scott, P. Emsbo, H. Thomas and J. Foster, *Economic Geology*, 2009, **104**, 635-668.
6. J. Woodhead, J. Hergt, S. Meffre, R. R. Large, L. Danyushevsky and S. Gilbert, *Chemical Geology*, 2009, **262**, 344-354.
7. P. J. Sylvester, *Laser ablation ICP-MS in the earth sciences: principles and applications*, Mineralogical Association of Canada, St. Johns. 2001.
8. P. M. Outridge, W. Doherty and D. C. Gregoire, *Spectrochimica Acta Part B*, 1997, **52**, 2093-2102.
9. J. Gonzalez, C. Liu, S.-B. Wen, X. Mao and R. Russo, *Talanta*, 2007, **73**, 567-576.
10. F.-X. D'Abzac, A.-M. Seydoux-Guillaume, J. Chmeleff, L. Datas and F. Poitrasson, *JAAS*, 2012, **27**, 108-119.
11. T. Hirata and Z. Miyazaki, *Analytical Chemistry*, 2007, **79**, 147-152.
12. A. Gusarov and I. Smurov, *Journal of Applied Physics*, 2005, **97**.
13. H.-R. Kuhn and D. Gunther, *Analytical Chemistry*, 2003, **75**, 747-753.
14. J. Koch, N. Feldmann, K. Jakubowski and K. Niemax, *Spectrochimica Acta Part B*, 2002, **57**, 975-985.
15. J. Koch, A. von Bohlen, R. Hergenroder and K. Niemax, *JAAS*, 2004, **19**, 267-272.
16. J. Kosler, M. Wiedenbeck, R. Wirth, J. Hovorka, P. J. Sylvester and J. Mikova, *JAAS*, 2005, **20**, 402-409.
17. E. F. Cromwell and P. Arrowsmith, *Analytical Chemistry*, 1995, **67**, 131-138.
18. S. Chenery, A. Hunt and M. Thompson, *JAAS*, 1992, **7**, 647-652.
19. R. Hergenroder, *JAAS*, 2006, **21**, 1016-1026.
20. R. Hergenroder, *JAAS*, 2006, **21**, 505-516.
21. R. Hergenroder, *JAAS*, 2006, **21**, 517-524.
22. H.-R. Kuhn and D. Gunther, *JAAS*, 2004, **19**, 1158-1164.
23. M. Loewen and A. Kent, *JAAS*, 2012, **27**, 1502-1508.
24. S. E. Jackson and D. Gunther, *JAAS*, 2003, **18**, 205-212.
25. S. P. Kelley and A. Fallick, *Geochimica et Cosmochimica Acta*, 1990, **54**, 883-888.
26. M. Guillong and D. Gunther, *JAAS*, 2002, **17**, 831-837.
27. T. Wagner, A. Boyce and A. Fallick, *Geochimica et Cosmochimica Acta*, 2002, **66**, 2855-2863.
28. I. Kroslakova and D. Gunther, *JAAS*, 2007, **22**, 51-62.
29. P. J. Sylvester, in *Laser-Ablation-ICPMS in the Earth Sciences: Current Practices and Outstanding Issues*, ed. P. J. Sylvester, Mineralogical Society of Canada, Vancouver. 2008, pp. 67-78.
30. L. Danyushevsky, P. Robinson, S. Gilbert, M. Norman, R. Large, P. McGoldrick and M. Shelley, *Geochemistry: Exploration, Environment, Analysis*, 2011, **11**, 51-60.
31. M. Gaboardi and M. Humayun, *JAAS*, 2009, **24**, 1188-1197.
32. D. A. Holwell, *Contributions Mineral Petrology*, 2011, **161**, 1011-1026.
33. J.-H. Yuan, X.-C. Zhan, C.-Z. Fan, L.-H. Zhao, D.-Y. Sun, Z.-R. Jia, M.-Y. Hiu and L.-J. Kuai, *Chinese Journal of Analytical Chemistry*, 2012, **40**, 201-206.
34. J. E. Gagnon, B. J. Fryer, I. M. Samson and A. E. Williams-Jones, *JAAS*, 2008, **23**, 1529-1537.
35. Y. Liu, Z. Hu, S. Gao, D. Gunther, J. Xu, C. Gao and H. Chen, *Chemical Geology*, 2008, **257**, 34-43.
36. M. Humayun, F. A. Davis and M. M. Hirschmann, *JAAS*, 2010, **25**, 998-1005.
37. H. P. Longerich, S. E. Jackson and D. Gunther, *JAAS*, 1996, **11**, 899-904.
38. R. Kovacs and D. Gunther, *JAAS*, 2008, **23**, 1247-1252.
39. D. Gunther and B. Hattendorf, in *Laser Ablation ICP-MS in the Earth Sciences: Princliples and Applications*, ed. P. J. Sylvester, Mineralogical Association of Canada, Ontario. 2001, pp. 83-91.
40. P. Waldner and A. D. Pelton, *Journal of Phase Equilibria and Diffusion*, 2005, **26**, 23-38.
41. M. Guillong, C. Latkoczy, J. H. Seo, D. Gunther and C. A. Heinrich, *JAAS*, 2008, **23**, 1581-1589.
42. P. R. Craddock, O. J. Rouxel, L. A. Ball and W. Bach, *Chemical Geology*, 2008, **253**, 102-113.
43. M. Guillong, H.-R. Kuhn and D. Gunther, *Spectrochimica Acta Part B*, 2003, **58**, 211-220.
44. A. J. G. Mank and P. R. D. Mason, *JAAS*, 1999, **14**, 1143-1153.
45. S. M. Eggins, L. P. J. Kingsley and M. Shelley, *Applied Surface Science*, 1998, **127-129**, 278-286.
46. R. Arevalo, J. Bellucci and W. McDonough, *Geostandards and Geoanalyical Research*, 2010, **34**, 327-341.